Radiative transfer models of water plumes in Ganymede's atmosphere Preparing SWI/JUICE observations

A&A, 711, A109 (2026)
https://doi.org/10.1051/0004-6361/202555992

Astronomy & Astrophysics

Radiative transfer models of water plumes in Ganymede's atmosphere

Preparing SWI/JUICE observations

T. Margheri[1,⋆], E. S. Wirström[1], P. Bjerkeli[1], L. Rezac[2], and P. Hartogh[2]

[1] Department of Space, Earth, and Environment, Chalmers University of Technology, 412 96 Gothenburg, Sweden
[2] Max-Planck-Institut für Sonnensystemforschung, Justus-von-Liebig-Weg 3, 37077 Göttingen, Germany

Received 17 June 2025 / Accepted 31 March 2026

ABSTRACT

Context. Detecting and characterising plumes that may insert subsurface water into the tenuous atmospheres of the icy Galilean moons is a key objective for the Submillimetre Wave Instrument (SWI) on board ESA's JUpiter ICy moons Explorer (JUICE) mission. However, faint spectral signatures and complex observational geometries during distant moon monitoring pose significant challenges.

Aims. Our aim with this study is to assess the feasibility of detecting water plumes on Ganymede with SWI during the planned moon monitoring observations while orbiting Jupiter. We investigated how observational geometry and plume physical properties might influence the spectral signatures of a gas-phase water plume observed by SWI.

Methods. We used the LIne Modelling Engine (LIME) software package, a 3D non-local thermodynamic equilibrium radiative transfer code, to simulate and analyse the ortho-H_2O spectral line at 557.936 GHz for different observational geometries. We focused on an observing distance of approximately 1.2×10^6 km from Ganymede, corresponding to the moon monitoring phase planned for SWI as part of the JUICE mission. We modelled key plume parameters, including temperature, production rate, and velocity fields, along with different SWI viewing geometries, to assess their impact on plume detectability and to develop strategies for optimising observations.

Results. Simulations indicate that SWI can detect water plumes on Ganymede under favourable conditions, even for water production rates as low as 10^{27} s^{-1}. Detection is most likely if the plume is observed at the limb of the moon or when located at 90° from the subsolar point. In these geometries, the plume contributes with strong emission line wings with temperature contrasts up to ~4 K for production rates around 10^{29} s^{-1}. Such line wings can be detected with a signal-to-noise ratio of 7 with a 10-minute integration using the high-resolution Chirp Transform Spectrometer backend of SWI during the modelled moon monitoring observations. Increased plume temperatures and velocity distributions enhance line intensity and broadening, potentially enabling plume identification even at lower production rates.

Key words. radiative transfer – space vehicles: instruments – planets and satellites: atmospheres – planets and satellites: individual: Ganymede – submillimeter: planetary systems

1. Introduction

Ganymede, the largest moon of Jupiter, is one of the primary targets to study for investigations into the habitability of our Solar System. Data from Galileo's magnetometer (Kivelson et al. 1996, 2002) and auroral emissions observed by the Hubble Space Telescope (HST) (Saur et al. 2015) suggest the presence of a subsurface saltwater ocean beneath Ganymede's icy crust. More recently, HST ultraviolet observations have provided the first detection of a tenuous water atmosphere (Roth et al. 2021) likely originating from surface ice sublimation. However, the presence of water vapour could also result from plume activity erupting from Ganymede's surface and potentially ejecting ocean material into space. Although direct and indirect evidence of water plumes on Ganymede is lacking, these phenomena have been observed on other icy moons, such as Europa (Roth et al. 2014; Sparks et al. 2016; Jia et al. 2018; Paganini et al. 2020) and Enceladus (Spahn et al. 2006; Waite et al. 2006; Hansen et al. 2006; Porco et al. 2006), suggesting that similar processes could also occur on Ganymede. Investigating the presence of water plumes would provide a means to probe the composition of internal liquid reservoirs and inform studies of the moon's potential to support life.

In order to study Jupiter and the Galilean icy moons, their atmospheric composition, and the possible presence of water plumes in their atmospheres, the European Space Agency (ESA) launched the Jupiter Icy Moons Explorer (JUICE) space mission in April 2023. JUICE is expected to arrive at Jupiter in 2031 and will later enter orbit around Ganymede (Fletcher et al. 2023). The Submillimeter Wave Instrument (SWI), one of the ten instruments on board JUICE, will be used to determine the composition of the moon's atmosphere, with its 29 cm diameter antenna. Notably, SWI will be able to detect rotational transitions of water and other molecular species in the atmosphere within the frequency range of 527–635 GHz and 1066–1286 GHz at a high spectral resolution of 10^5–10^7. Throughout the tour of Jupiter, Ganymede will be observed from various distances, initially from more than 1.9×10^7 km, where the SWI beam (440″ FWHM at 557.936 GHz) will not be able to resolve the moon, and towards the end of the mission from close orbit, at an altitude of 500 km (Grasset et al. 2013).

To assess the observability of water plumes with SWI, inform science planning, and eventually support the interpretation of

⋆ Corresponding author: margheri@chalmers.se

future measurements, we simulated the 557.936 GHz ground-state rotational transition of ortho-water, a highly sensitive tracer of cold low-density water vapour. We investigated how a single localised water plume affects the observed line profile, depending on its position relative to the subsolar point (SSP) and the observing geometry. For this purpose, we built upon the 3D non-local thermodynamic equilibrium (non-LTE) model of Ganymede's atmosphere developed by Wirström et al. (2020), incorporating a parametrised conical plume defined by a water production rate, gas temperature, and outflow velocity.

In Sect. 2, we introduce the atmospheric model used for the simulations. We describe the composition and physical processes occurring in Ganymede's atmosphere and follow it with an overview of the radiative transfer code applied in non-LTE conditions. We then explain how the plume is incorporated into the model and outline the different geometric configurations used to test its detectability. In Sect. 3, we present the results of the simulations. We first show the base model case, with the plume placed at different locations on the moon and observed from various phase angles. Then we explore how the plume signal changes when varying key physical parameters such as the water production rate, gas temperature, and velocity distribution. Finally, in Sect. 4, we discuss the implications of our findings for planning SWI observations, identifying favourable conditions for detecting water plumes and suggesting strategies for observing both transient and persistent plume activity with the SWI instrument on JUICE.

2. Modelling Ganymede's atmosphere with a plume

2.1. Atmospheric composition and processes

The atmosphere of Ganymede is one of the most complex among the moons of our Solar System. As the only known satellite to have an intrinsic global magnetic field (Gurnett et al. 1996; Kivelson et al. 2002), embedded within the larger magnetosphere of Jupiter, the interaction of these fields shapes the morphology of the atmosphere (Hall et al. 1998; McGrath et al. 2007; de Kleer et al. 2023).

The chemical composition of Ganymede's atmosphere should, to some extent, reflect that of its surface, which largely consists of water ice (Ligier et al. 2019; Bockelée-Morvan et al. 2024), as also observed on the other icy Galilean moon, Europa (Pilcher et al. 1972; Showman & Malhotra 1999; Hansen & McCord 2004). In addition, similar to the case of Europa, the presence of H_2O_2 surface ice has been confirmed by Trumbo et al. (2023). The primary atmospheric constituents are water-related species, such as H_2O molecules, non-condensing O_2 and H_2 molecules, as well as highly reactive dissociation products such as atomic O, H and OH. These molecules are liberated from Ganymede's surface and introduced into the atmosphere through sputtering and sublimation processes (Vorburger et al. 2022).

Sputtering is driven by the energetic Jovian plasma, which interacts with Ganymede's intrinsic magnetic field (Poppe et al. 2018). Sputtering intensity follows the distribution of the precipitating plasma, particularly at the poles where plasma fluxes are highest. Sublimation process occurs primarily near the SSP, where surface temperatures reach 80–150 K, causing water ice to release water vapour into the atmosphere with an exponential dependence on temperature (Spencer 1987; Orton et al. 1996; Roth et al. 2021).

Both O_2 and H_2 are produced through irradiation, where energetic Jovian plasma ions and electrons bombard Ganymede's surface (Turc et al. 2014). These species then diffuse outwards from the surface over time. Highly reactive species such as O, H, and OH are also formed through surface irradiation, but due to their chemical reactivity, they typically recombine within the ice lattice and do not diffuse into the atmosphere. However, these species are generated primarily in the atmosphere through the dissociation of parent molecules, such as H_2O, O_2, and H_2.

2.2. Modelling the atmosphere

As explained in the previous section, Ganymede's atmosphere is influenced by both sublimation and sputtering processes. At the SSP, where sublimation is most effective, the increased local density amplifies collisional interactions, enabling the atmosphere to be approximated as in local thermodynamic equilibrium (LTE) up to altitudes of around 150–200 km. At higher latitudes (above 45°) and altitudes above 200 km, the atmosphere becomes rarefied, and collisions less frequent, leading to a transition to non-LTE where excitation temperatures of individual water transitions substantially differ from kinetic temperatures (cf. Fig. 3 of Wirström et al. 2020). To properly simulate H_2O spectral lines in Ganymede's atmosphere, accounting for spatially asymmetric water and temperature distribution, we made use of the code LIME Brinch & Hogerheijde (2010), capable of performing 3D radiative transfer in a non-LTE state. For this study, we employed version 1.9.5 of LIME. The code requires input in the form of analytical functions or numerical descriptions of the density, temperature, molecular abundance, gas-to-dust ratio, and velocity fields. LIME constructs an unstructured Delaunay grid through sampling weighted by the model density and calculates the rotational level populations at each grid point iteratively, taking into account the local temperature, density, and radiation field. The code then performs ray-tracing to generate the final data cube, which is output as a FITS file. For all models presented in this work, we use 14 iterations and a total of 100 000 grid points. Convergence of the level populations was verified by comparing models run with 14 and 28 iterations, while keeping all other parameters fixed. These tests showed no significant changes in the spectra or in the level populations as a function of radius. Additional tests, using an older LIME version (v1.4.3) and an increased number of grid points equal to 200 000, confirmed no differences in the results. In this work, we focused on modelling the rotational line of the ground-state ortho-water transition H_2O (1_{10}–1_{01}) at 556.936 GHz higher-state energy 61 K), which will provide the strongest spectroscopic signals and is thus considered the most effective for large-scale mapping and monitoring of water distribution.

The background density and temperature distributions were derived from the kinetic model by Marconi (2007), which provides an overview of Ganymede's atmospheric composition. The details of the atmospheric model are described in Wirström et al. (2020), hereafter referred to as Paper I, and are summarised in Table 1. The surface temperature distribution is assumed to correspond to the atmospheric temperature at the base of the atmosphere, as in Paper I, peaking at 150 K at the SSP and decreasing to 122 K on the night side.

Given that vertical and horizontal velocities of water in Ganymede's lower atmosphere are estimated to be below 100 m/s (Marconi 2007), all macroscopic (translational) velocities are set to zero in the radiative transfer calculations. The Doppler parameter, representing additional non-thermal ('turbulent') broadening, is also set to zero. For the collisional excitation, only collisions with water are taken into account, and the H_2O–H_2O collision rates from Buffa et al. (2000) are adopted, as in Paper I. We note that new H_2O-H_2O collision rates have recently

Table 1. Parameters for Ganymede's atmosphere model.

Parameter	Value	Reference
Ganymede radius	2634 km	1
Atmosphere height	450.5 km	1
Outer model radius	3500 km	1
$T_{kin,max}$ (H_2O)	150 K	1
n_{max} (H_2O)	1×10^9 cm^{-3}	1
Coll. partner	H_2O	2
H_2O ortho/para	3	2
Gas-to-dust ratio	100	1
$T_{background}$	2.73 K	1
Total grid points	100 000	1
Grid weight	$\left(\frac{n}{n_0}\right)^{0.2}$, $n_0 = 10^9$ cm^{-3}	1

Notes. (1) Wirström et al. (2020); (2) Buffa et al. (2000).

Table 2. Parameters of the base model for the water plume.

Geometry parameters	Base model value
Plume opening angle (θ)	90°
Vent radius (r_{vent})	10 m
Temperature (T_{plume})	150 K
Exit radial velocity (v_{exit})	1 km s^{-1}
LIME parameters	
Water production rate (Q)	1×10^{29} mol s^{-1}
Temperature (T_{plume})	150 K
Macroscopic velocity dispersion (σ)	0 km s^{-1}

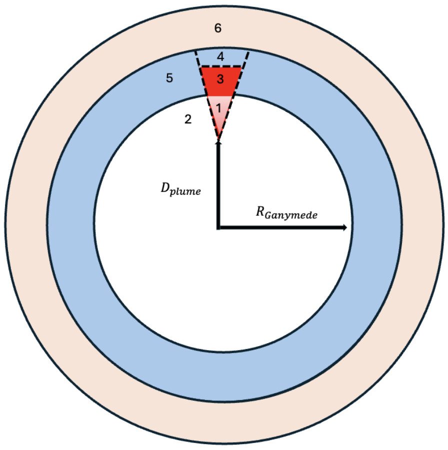

Fig. 1. Schematic representation of the water plume model divided into six regions with distinct molecular densities and temperatures. The size of Region 1 is exaggerated for clarity.

Table 3. Density and temperature in the LIME regions.

Region	n (cm^{-3})	T (K)
1	10^{22}	122–150$^{(a)}$
2	10^{22}	122–150$^{(a)}$
3	n_{plume}	T_{plume}
4	10^2–$10^{9(a)}$	90–150$^{(a)}$
5	10^2–$10^{9(a)}$	90–150$^{(a)}$
6	10^{-20}	2.73

Notes. $^{(a)}$ Wirström et al. (2020).

been calculated by Mandal & Babikov (2023) and Mandal et al. (2024). These are more complete, including a larger number of levels and transitions for the kinetic temperature range concerned here ($\lesssim$150 K). However, using these updated rates does not significantly affect the excitation or the modelled line profiles of the ground-state 557 GHz line, which is the focus of our study.

2.3. Modelling the water plume

In order to investigate how the presence of a water-dominated plume would manifest in SWI mapping observations, we incorporated a simplified functional representation of a water plume into the atmospheric model. A single plume source with a circular vent aperture is considered, oriented perpendicularly to Ganymede's surface and releasing exclusively water vapour in the shape of a truncated cone. The geometry of the plume is defined by a set of physical parameters that include the opening angle of the plume, the radius of the vent, the gas kinetic temperature, and the exit radial velocity. These parameters were used to calculate both the height and the volume of the conical plume (see first part of Table 2).

The modelled water gas properties inside the plume are described by the LIME parameters, as summarised in the second part of Table 2. For any chosen set of plume geometry parameters, the water production rate (number of water molecules expelled per second) determines the plume's water content and is used to compute the average water density, which serves as input for the LIME model. This rate is of particular importance for assessing plume detectability because for Ganymede there are no constraining observations, and plausible values may span several orders of magnitude. For the present simulations, the height of the plume is set by choosing an exit radial velocity of about 1 km/s, which is about twice the rms velocity of water gas at 150 K.

From pure energy conservation of particles with velocity v_{tot} at the surface, the height of the plume can be roughly estimated as

$$h_{plume} = \frac{v_{tot}^2}{2g_{GAN}}, \tag{1}$$

with g_{GAN} representing the surface gravity of Ganymede in m/s^2. For our base model, this expression yields a plume height of approximately 308 km. The density of water molecules within the plume, $n_{H_2O,plume}$, is then given by the following expression:

$$n_{H_2O,plume} = \frac{Q \cdot 2t}{V_{plume}}, \tag{2}$$

where Q is the water production rate in mol s^{-1}, $2t$ is the lifetime of the plume in s, and V_{plume} is the volume of the plume in m^3, calculated as the difference between the volume of the entire cone and the volume of the conical region below the surface of Ganymede. As shown in Equation (2), a higher production rate corresponds to a larger number of molecules being ejected within the same time frame, thereby increasing the molecular density within the plume and enhancing its detectability.

The water plume model is illustrated in Figure 1. Using the LIME code, we structured the model into six distinct regions with varying densities and temperatures. These regions and their corresponding physical properties are summarised in Table 3.

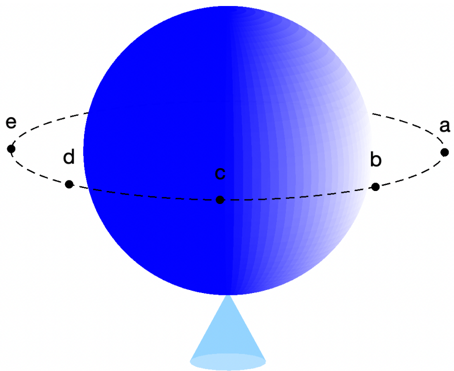

Fig. 2. Illustration of SWI viewing geometry in relation to the SSP for model CasesIII a, b, c, d, e with a plume at 90°. For Case a, SWI observes in the nadir direction, corresponding to a phase angle of 0°, and it increases in steps of 45° to the phase angle 180° in Case e. Note that the sizes of Ganymede, the plume, and the SWI orbit are not to scale.

Regions 1 and 3 represent the volumes within the plume, where the density of water molecules is determined by the chosen production rate, as described in Equation (2). For the geometry we have assumed, the height of the inner cone is 20 meters, which means that Region 1 can be considered small enough to not significantly contribute to the overall line profile. Region 2 corresponds to the solid moon itself, and as in Paper I, its physical properties are chosen to ensure that no photons propagate through the surface and that it is treated as a perfect absorber that emits at the local surface temperature. Region 4 and Region 5 cover the volume of the exosphere outside the plume, where the temperature and density have the same distribution as in Paper I. Region 6 represents the volume outside the exosphere, above 450.5 km altitude, where the density of the molecules drops significantly to 10^{-20} cm^{-3}, and the temperature remains constant at 2.73 K. Since we do not have any detailed information about water plumes on Ganymede we consider this simple model sufficient for this SWI sensitivity study.

2.4. Geometries of the model test cases

To analyse how the presence of a water plume could be identified in SWI observations, we performed different test cases by varying the SWI observing angle and the relative position of the plume with respect to the SSP. The location of the plume is defined by a plume rotation angle in the plane of Ganymede's rotation axis (the z-axis) and the latitude relative to the SSP, where 0° corresponds to a plume at the SSP and 90° to a plume at the south pole. An example of a test case studied is shown in Figure 3, where the plume is positioned at 90°relative to the SSP (illustrated by the spotlight on the left side of the moon). The SWI observations are then modelled from different phase angles in the equatorial plane of Ganymede where Case a corresponds to 0°, Case b to 45°, Case c to 90°, Case d to 135°, and Case e to 180°, as illustrated in Fig. 2. All the modelled test cases in terms of plume and SWI geometries relative to the SSP are summarised in Table 4. In this paper, we focus on a single observation distance of approximately 1.2×10^6 km from Ganymede, which corresponds to CaseIII in Paper I. From this distance, five-by-five on-the-fly mapping with half-beam-spacing is expected to be an important observation design for SWI. Such maps are representative of the daily moon-monitoring observations planned during the journey of JUICE in the Jupiter system until entering orbit around Ganymede. This setup provides an initial test framework to evaluate how a single plume affects SWI observations at a moderate resolution before extending modelling to closer distances or more complex scenarios. For a more in-depth discussion on the model's limitations, we refer the reader to Sect. 4.

Table 4. Overview of the modelled test cases.

Case	Plume	SWI	ΔT_{max} (K)	Line	Δ(S/N)$_{10\,min}$
III a0	0°	0°	3	Centre	5
III b0	0°	45°	2	Centre	3
III c0	0°	90°°	2	Wings	3
III d0	0°	135°	<1	Centre	–
III a45	45°	0°	3	Centre	5
III b45	45°	45°	2	Centre	3
III c45	45°	90°	2	Wings	3
III d45	45°	135°	<1	Centre	–
III a90	90°	0°	3	Wings	5
III b90	90°	45°	3	Wings	5
III c90	90°	90°	4	Wings	5
III d90	90°	135°	3	Wings	5
III e90	90°	180°	4	Wings	7
III b180	180°	45°	<1	Centre	–
III c180	180°	90°	4	Centre	7
III d180	180°	135°	2	Centre	3
III e180	180°	180°	3	Centre	5

Notes. The table lists the modelled test cases, with their observing geometry properties, the maximum difference between the modelled line intensities with and without a plume (ΔT_{max}), the region in which part of the line shape the maximum difference occurs, and the signal-to-noise ratio of this modelled maximum difference Δ(S/N) for a 10-minute integration.

3. Results

The following section presents the results of our simulations, starting with the description of the base model for all tested geometries. We then proceed to explore how variations in key physical parameters affect the detectability of the plume, focusing on the most promising geometries.

For each test case, we use LIME to compute high-spatial-resolution spectral maps for the H_2O (1_{10}–1_{01}) line. To simulate expected SWI observations, we applied a 2D Gaussian convolution with an FWHM of 440″, generating an oversampled map with a pixel size of 6 arcsec, much smaller than the SWI beam. From these processed maps, we then extracted five-by-five spectral maps where neighbouring positions are separated by 1429.5 km, 12% more than half the beamwidth. This stretched spacing ensures that map positions at the limb are shifted to an atmospheric altitude of 225 km, which corresponds to half the height of the modelled atmosphere, and in the base model to 72% of the plume height.

The five-by-five maps are displayed from Figures 3 to 10. The presented maps show baseline-subtracted spectra overlaid on a moment-zero map (integrated intensity) where regions ranging from light cyan to dark blue correspond to increasing absorption, and regions ranging from light yellow to dark red correspond to increasing emission. The moment-zero map is presented at

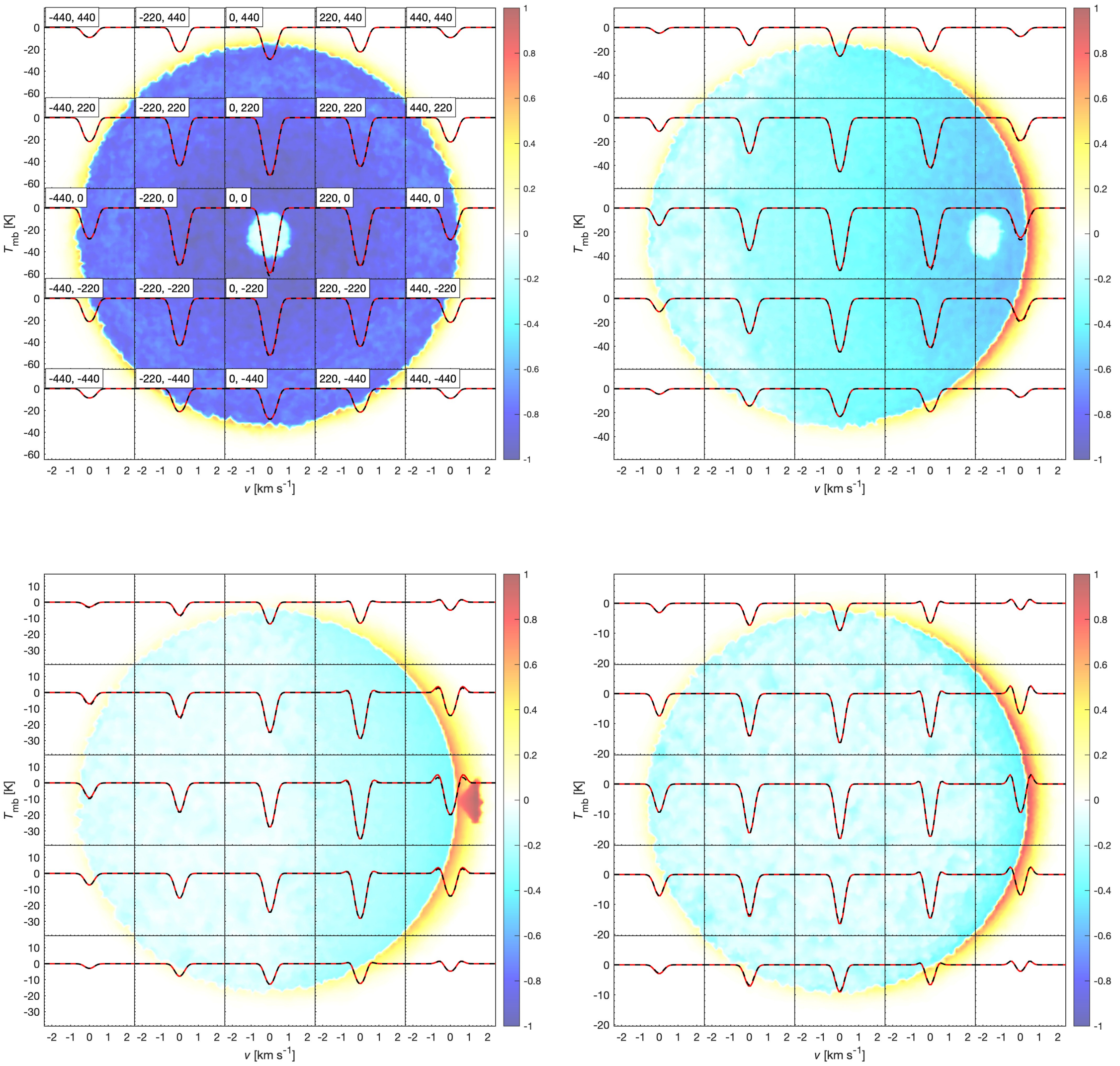

Fig. 3. Five-by-five maps of Ganymede with the plume originating at the SSP. The spectral lines are baseline-subtracted and overlaid on a moment zero map of the full resolution plume model. The dashed black line results from the atmosphere model without the plume, while the solid red line corresponds to the base model with the plume. The y-axis of the spectra represents the main beam brightness temperature after continuum subtraction, i.e., $T_{\rm mb} = T_L - T_{\rm cont}$. The *upper-left panel* shows CaseIII a0, where the SWI instrument is positioned at a phase angle of 0° with respect to the SSP. The *upper-right panel* displays CaseIII b0, where the SWI is located at a phase angle of 45°. The *lower-left panel* corresponds to CaseIII c0, with the SWI at a phase angle of 90°, and the *lower-right panel* presents CaseIII d0, where the SWI is situated at a phase angle of 135°. The colour bar indicates the integrated intensity T_{int}, normalised to the absolute maximum value, so the maximum value of the colour bar corresponds to 1. The map coordinates in all panels are the same as in CaseIII a0 (*upper-left panel*).

full resolution, where each pixel corresponds to 6 arcsec. The moment zero colour map is normalised to the highest or lowest integrated intensity, depending on which has the greatest absolute value. Consequently, the colours in these figures vary throughout the paper. White areas indicate regions where there is neither absorption nor emission. The amplitude of the simulated spectral lines is presented on different scales, depending on the depth of the absorption line or its emission, which varies case by case.

In Sect. 3.1, we analyse the spectral maps obtained for different SWI viewing angles, considering a fixed water production rate. These maps illustrate the contribution of the plume to the observed water spectral lines and help identify the geometries that maximise detectability. In Sect. 3.2, we investigate the influence of different physical parameters on the plume's spectral signature. We systematically vary the water production rate (Sect. 3.2.1), the plume gas temperature (Sect. 3.2.2), and the plume gas velocity (Sect. 3.2.3). By assessing how these factors modify the spectral features, we aim to constrain the conditions under which a water plume on Ganymede can be most effectively observed. This structured approach allows us to understand the impact of both observation geometry and physical properties on the detectability of the plume, providing a comprehensive picture of its spectral behaviour.

3.1. Base model

In this section, we present the results of the base model, where the water production rate is fixed at 1×10^{29} s^{-1}, comparable to the values observed for the plume activity of Europa (Paganini et al. 2020). This corresponds to a plume water density $n_{\rm plume} \simeq 8 \times 10^9$ cm^{-3}, which is high enough for the excitation to be in LTE throughout the plume. The other parameters of the modelled plume were chosen on the basis of prior

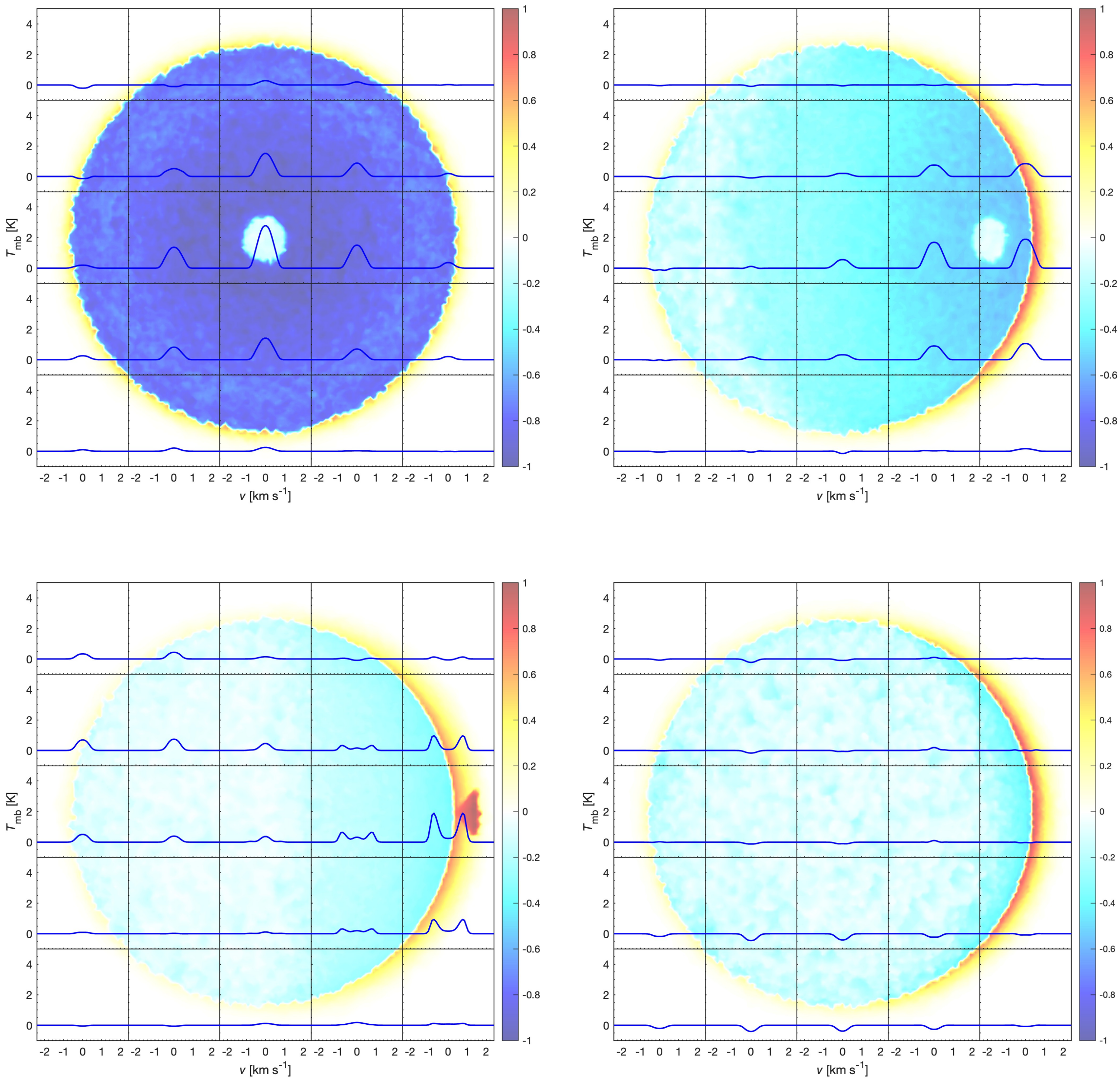

Fig. 4. Same maps as in Figure 3 but with the blue spectrum now representing the difference between the plume-affected spectrum (solid red line) and the atmospheric spectrum without the plume (dashed black line). The maximum difference is observed in CaseIII a0 (*upper-left panel*), where the temperature variation reaches 3 K. In the *lower-left panel*, the shape of the blue spectrum is influenced by the presence of emission wings in CaseIII c0. The colour bar indicates the integrated intensity, T_{int}, normalised to the absolute maximum value. The map coordinates in all panels are the same as the *upper-left panel* in Figure 3.

studies of plume dynamics on icy moons. Specifically, the vent radius is set to r_{vent} =10 m, following the model proposed by Dayton-Oxland et al. (2023), which assumes a single plume source with a circular aperture normal to the surface.

For the exit velocity, Hubble Space Telescope (HST) observations suggest a value of approximately 700 m s^{-1} for Europa's plumes (Roth et al. 2014), while Cassini data indicate velocities around 500 m s^{-1} for Enceladus (Tian et al. 2007). Considering Ganymede's larger surface gravity compared to Europa (and Enceladus), we adopted a slightly higher exit velocity of 1 km s^{-1}. All the cases and their corresponding observing geometries are summarised in Table 4. The maximum temperature difference, $\Delta T_{\max}$, between the spectrum with the plume and the spectrum without the plume is always computed at the spatial location centred on the plume and indicated in the fourth column of the table. The line position specifies if the maximum temperature difference occurs at the centre of the spectral line or in the wings, based on the shape of the difference spectrum. Finally, the last column lists $\Delta(S/N)_{10\,\min}$ the signal-to-noise ratio of the maximum difference spectrum for an integration time of 10 minutes. This estimate assumes a system temperature of 3000 K, a spectral resolution of 100 kHz, and dual polarisation.

3.1.1. Plume located at the SSP

Figure 3 shows the spectral map for a plume located at the SSP, with results from different phase angles. When SWI is observing from 0° with respect to the SSP (CaseIII a0), the water line is only seen in absorption. The solid red line represents the model including the plume, while the dashed black line corresponds to the atmosphere model without the plume. We can discern that the solid red line shows a less deep absorption than the dashed black line, especially at the centre position. This indicates that the plume is reducing the depth of the absorption lines due to its emission at approximately the same temperature as the surface, with only the uppermost part of the atmosphere contributing to

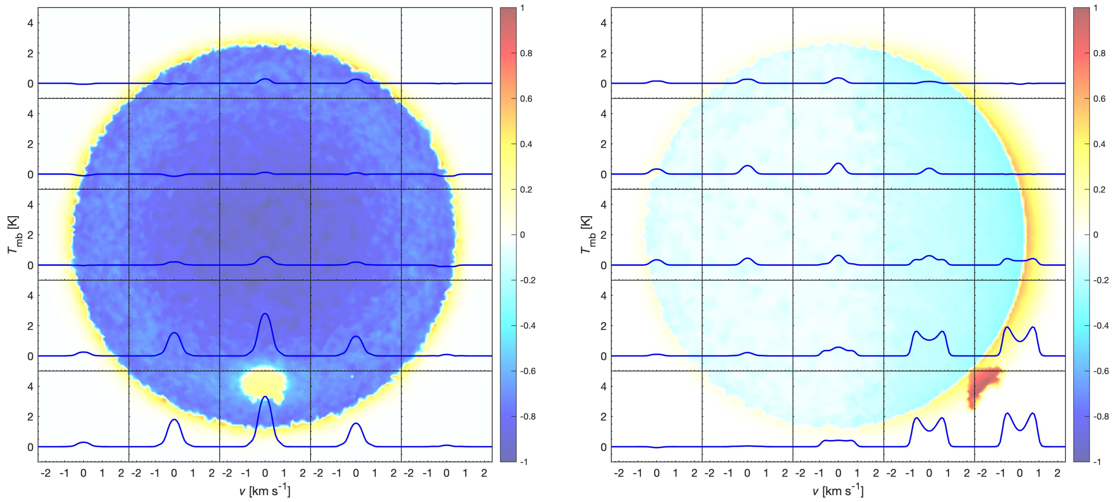

Fig. 5. Difference spectra for a plume located at 45°obtained by subtracting the no-plume case from the plume-affected case. The *left panel* corresponds to CaseIII a45, while the *right panel* corresponds to CaseIII c45, with SWI positioned at phase angles of 0°, and 90°, respectively. The colour bar indicates the integrated intensity, T_{int}, normalised to the absolute maximum value. The map coordinates in all panels are the same as the *upper-left panel* in Figure 3.

the absorption, as can be seen in the background high-resolution colour scale map. When plotting the difference between the two spectra (see Figure 4), we observed that the plume introduces a shift of approximately 3 K in the central absorption feature, showing a less pronounced absorption.

The modelled observations at 45°(CaseIII b0) show a very similar trend to the 0° case (CaseIII a0), where the spectral line remains in absorption and and the presence of the plume leads to a slightly reduced line depth, with a temperature difference of up to 2 K (see the upper-right panel of Figure 4). As the viewing angle increases, emission wings start to appear in both spectra towards the SSP side of the map, especially at 90° (CaseIII c0). In this geometry, the emission wings are more pronounced in the plume case, by up to 2 K, highlighting the additional contribution from the plume within the instrument beam at this perpendicular view. Note that since the plume water gas has no velocity offset from the general atmosphere in this version of the model, the position of the wings are not shifted relative to the general atmosphere. The effect of moving plume gas on observed line profiles is explored in Sect. 3.2.3. At 135° (CaseIII d0), the plume lies behind the limb and no longer contributes to the observed line profile. The wings that remain visible in both spectra are instead due to atmospheric emission near the limb, where the line of sight passes through a more extended column of water vapour (see lower-right panel of Figure 4).

3.1.2. Plume located at 45° from the SSP

When the plume is positioned at 45° from the SSP, the spectral features in the map display an overall trend similar to the SSP case, with line wings appearing when the SSP is observed near the limb (see Figure A.1). The maps in Figure 5 show the difference spectra for the two most relevant cases: CaseIII a45 and CaseIII c45. At a phase angle of 0° (CaseIII a45), the plume reduces absorption by approximately 3 K, consistent with the SSP case. At 90° (CaseIII c45), the difference spectra display a characteristic double-peak pattern, with emission contributions from the plume of up to 2 K in the lower-right corner of the map, closest to the plume. Cases at 45° and 135° (CaseIII b45 and CaseIII d45) are not shown here, as they do not provide additional insights. Indeed, in CaseIII b45, the spectral profiles are similar to CaseIII a45, with a maximum temperature difference of 2 K. In CaseIII d45, the plume has only a minimal effect on the spectra (see Table 4).

3.1.3. Plume located at 90° from the SSP

The results for a plume positioned at 90° from the SSP, at the south pole, are shown in Figure A.2. For SWI position at 0° (CaseIII a90), the absorption line is still prominent; however, the presence of the plume is clearly indicated by the emission wings in the spectra observed towards the south pole limb, where the plume originates. The same trend is also observed for a phase angle of 45° (CaseIII b90) and remains consistent in all other cases: 90° (CaseIII c90), 135° (CaseIII d90), and 180° (CaseIII e90). However, in the cases of 90° (CaseIII c90) and 135° (CaseIII d90), emission wings are also present near the SSP region at the right limb of the moon. The most representative cases are CaseIII c90 and CaseIII e90, with SWI located at a phase angle of 90° and 180°. The difference spectra are shown in Figure 6, highlighting an emission of approximately 3.5 K for CaseIII c90 and 4 K for CaseIII e90 (see Table 4). While the magnitude of this difference is comparable to the previously described cases, the distinction from the non-plume case is much more pronounced here, as the atmosphere by itself does not contribute with any emission wings at all. Since all other cases show similar spectral behaviour, we chose to show only the difference spectrum for these two cases.

3.1.4. Plume located at 180° from the SSP

For the case with a plume located 180° from the SSP, SWI observations from a 0° phase angle are not expected to show any plume signatures so we do not present resulting maps for this case. Instead, we focus on the observations at 45°, 90°, 135°, and 180° phase angles. When the viewing angle are 90° (CasesIII c180), 135°(CaseIII d180), and 180° (CaseIII e180), the emission wings become visible in the region where the plume originates (see Figure A.3). The difference spectra for the two most relevant cases, CaseIII c180 and CaseIII e180, are

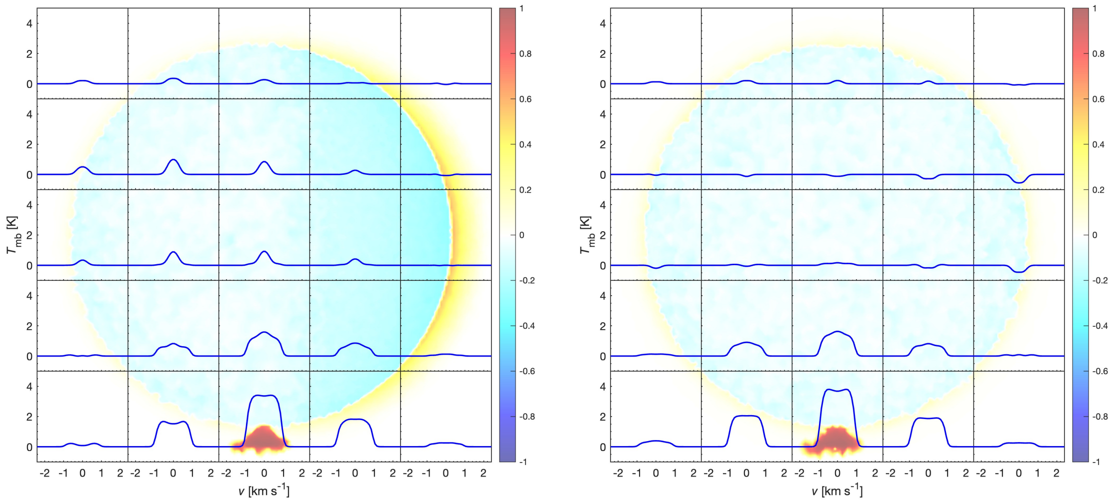

Fig. 6. Difference spectra for a plume located at 90°obtained by subtracting the no-plume case from the plume-affected case. The *left panel* corresponds to CaseIII c90, while the *right panel* corresponds to CaseIII e90, with SWI positioned at phase angles of 90°, and 180°, respectively. The colour bar indicates the integrated intensity, T_{int}, normalised to the absolute maximum value. The map coordinates are the same as the *upper-left panel* in Figure 3.

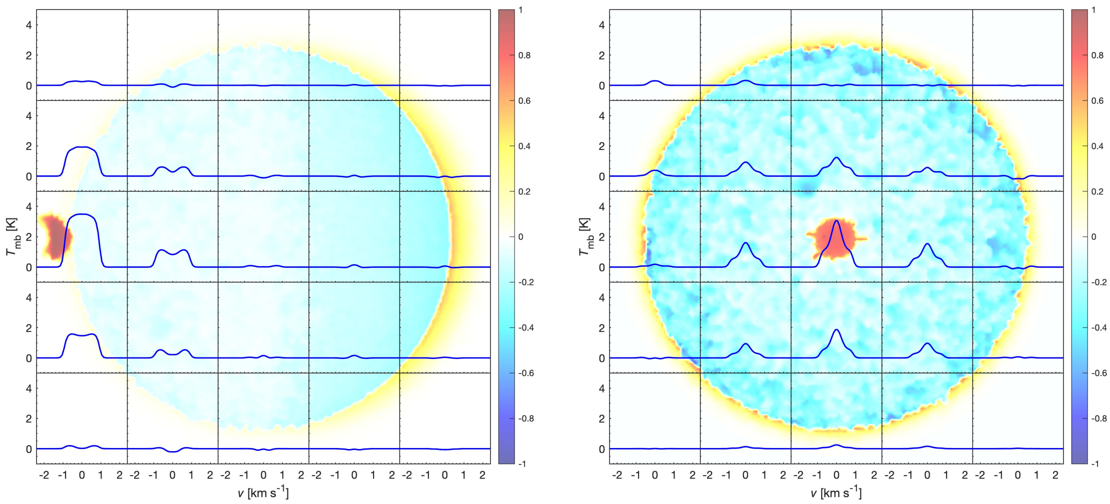

Fig. 7. Difference spectra for a plume located at 180°obtained by subtracting the no-plume case from the case with a plume. The *left panel* corresponds to CaseIII c180, while the *right panel* is for the CaseIII e180, with SWI positioned at phase angles of 90°, and 180°, respectively. The colour bar indicates the integrated intensity, T_{int}, normalised to the absolute maximum value. The map coordinates in all panels are the same as the *upper-left panel* in Figure 3.

displayed in Figure 7. For CaseIII c180, the difference spectrum reveals a peak temperature difference of approximately 3.5 K (see Table 4), marking this configuration as the one with the most pronounced plume signature for this geometry. CaseIII e180 displays a distinct spectral shape due to the combined effects of reduced central absorption (up to 3 K of difference) and weak emission wings (only ~1 K). CaseIII d180 presents a similar but less pronounced behaviour, with a difference up to 2 K. We do not consider this case particularly informative, and it is therefore not shown. CaseIII b180 is also negligible, as no significant differences are observed between the spectra with and without the plume.

3.2. Plume parameter exploration

In this section, we explore how different plume parameters influence the resulting spectral maps. These tests help us understand how sensitive the observed spectral line variations are to the main physical properties of the plume and provide insight into how variations in these properties affect the detectability with SWI.

3.2.1. Water production rate

In the base model, we assume a plume water production rate of the same order as that observed on Europa. However, conditions on Ganymede may differ significantly, potentially resulting in a very different production rate. We investigate its impact by modelling and comparing four different rates: $Q_1 = 10^{27}$, $Q_2 = 10^{28}$, $Q_3 = 10^{29}$ (base model), and $Q_4 = 10^{30}$ molecules s^{-1}, for the geometric configuration in which SWI is positioned at the SSP with respect to a plume located at the south pole, corresponding to CaseIII a90. This geometry was chosen because it provides one of the most favourable conditions for detecting a potential plume with SWI, as seen in the previous section.

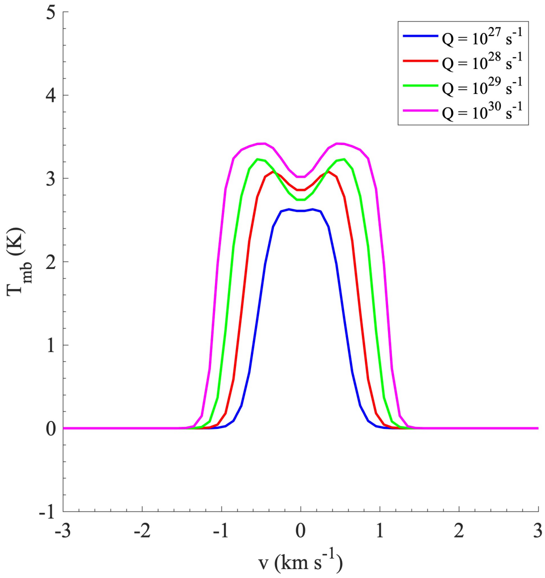

Fig. 8. Difference spectra for the map position centred on the plume (0,–440) for CaseIII a90 (i.e. observing from the zero phase angle with the plume at the south pole). The different colours represent different water production rates, ranging from 10^{27} to 10^{30} s^{-1}.

As the plume density scales linearly with the production rate (for kept plume geometry and temperature), excitation is expected to start deviating from LTE at some lower production rate. Indeed, while the excitation temperature of the 557 GHz line is still thermalised to within T_{plume}±2 K for $Q2$; at $Q1$, when $n_{plume} \simeq 8 \times 10^7$ cm^{-3}, it deviates by up to 20 K, confirming non-LTE excitation. The optical depth through the upper part of the plume, as modelled in LIME, shows a clear linear trend with the production rate, with optically thin emission only produced for production rates below 10^{27} s^{-1}. This trend is also reflected in the difference spectra towards the south pole region, as seen in Fig. A.4. As the production rate increases, the difference spectrum, shown in Fig. 8, foremost broadens, with the saturated line centre only increasing slightly in intensity and emission in the line wings becoming more dominant, an effect that is sometimes referred to as optical depth broadening. The maximum temperature difference only rises from approximately 2.6 K for the lowest production rate (Q_1) to nearly 3.4 K for the highest (Q_4). Note that the broadening, resulting in emission wings in the spectra, occurs already for production rates above 10^{27} s^{-1}; see Figure A.4.

3.2.2. Plume gas temperature

For the base model we choose a plume gas temperature (150 K) similar to the SSP surface temperature, which is also close to the water ice desorption temperature under interstellar conditions (Fraser et al. 2001). However, a liquid subsurface ocean of Ganymede needs to have temperatures above ~250 K, exact temperature depending on salinity (Vance et al. 2021), while adiabatic cooling is expected to rapidly lower the temperature of plume gas as it expands from a vent on an icy moon surface (Tseng et al. 2022). As discussed in Sect. 2.2, the overall water excitation is only thermalised at T_{kin} in the densest region of the atmosphere, but this is also true for the base model plume gas, at a density of $\sim 8 \times 10^9$ cm^{-3}. To investigate the effect of a warmer plume on the observed spectra, we analysed three different cases where the plume temperature was set to 300 K: CaseIII a0, CaseIII c0, and CaseIII c90. As shown in Figure 9, the plume contributes with a significant amount of emission to the line profiles towards the plume positions as compared to the base model, causing intensity differences of up to 10–20 K depending on the location of the plume and the observing geometry. In particular, the emission wings appear much more pronounced in the beam averaged spectra covering the higher temperature plume. This demonstrates that a higher plume temperature enhances the detectability of the plume.

Motivated by plume expansion models predicting rapid adiabatic cooling (Tseng et al. 2022), we explored the impact of lower plume temperatures by running an additional set of models with a plume gas temperature of 75 K. This value is representative of the cooler plume core expected at larger distances from the vent. In this regime, the reduced kinetic temperature leads to lower excitation of the rotational levels and since the plume temperature has an impact on its height through the total gas velocity in our geometrical model, the extension and beam filling of the 75 K plume is smaller, as seen in Fig. 9, thus contributing less to the observed lines. As shown in Fig. 9, the plume signal is strongly diminished at 75 K. In CaseIII a0, plume rather appears in stronger absorption against the SSP moon background than the surrounding atmosphere, slightly increasing the depth of the absorption. This occurs because the plume gas is significantly colder than the background emission. Instead for CaseIII c0 and CaseIII c90, the emission wings are present but at very low intensity, with <1 K difference signal.

3.2.3. Plume gas velocity

In addition to temperature, the velocity of the gas within the plume also plays a crucial role in shaping the observed spectral features. The base model does not take into account any radial molecular movement for the purpose of the radiative transfer, even if an exit velocity of 1 km s^{-1} is adopted to set the modelled height of the plume. It neither takes into account any random macroscopic gas motions, as set by the velocity dispersion, σ. Here we therefore extend our analysis to explore how different plume velocity configurations may impact the spectral signatures, this by considering the two simplified cases that either there is an overall radial movement of the gas or there is no radial movement but a large-scale velocity dispersion. Neither case is physically viable but serves to illustrate maximum effects on observed line profiles. To explore this, we considered three cases when the plume is located at the SSP but observed from different phase angles: CaseIII a0 and CaseIII b0, both characterised by a radial plume velocity of 500 m s^{-1}, and CaseIII c0, where a macroscopic velocity dispersion σ of 500 m s^{-1} was applied for the plume gas. The corresponding spectra are shown in Figure 10.

In the upper-left panel, we present CaseIII a0, where a radial velocity of 500 m s^{-1} in the plume is assumed. As expected from the Doppler effect, the spectral line centre of the plume (solid red line) is shifted relative to the one without the plume (dashed black line). In addition, the plume adds emission to the beam, which results in a reduction of the absorption line depth. A similar behaviour is observed in the centre left panel, corresponding to CaseIII b0, which is also characterised by a radial velocity of 500 m s^{-1}. In this case, the spectral shift induced by the plume is smaller compared to that seen in CaseIII a0, with the velocity shift being approximately 0.3 km s^{-1} at the maximum absorption. However, it should be noted that the absorption depth in the spectrum with the plume is less pronounced in CaseIII b0, as clearly shown by the difference spectra (upper- and

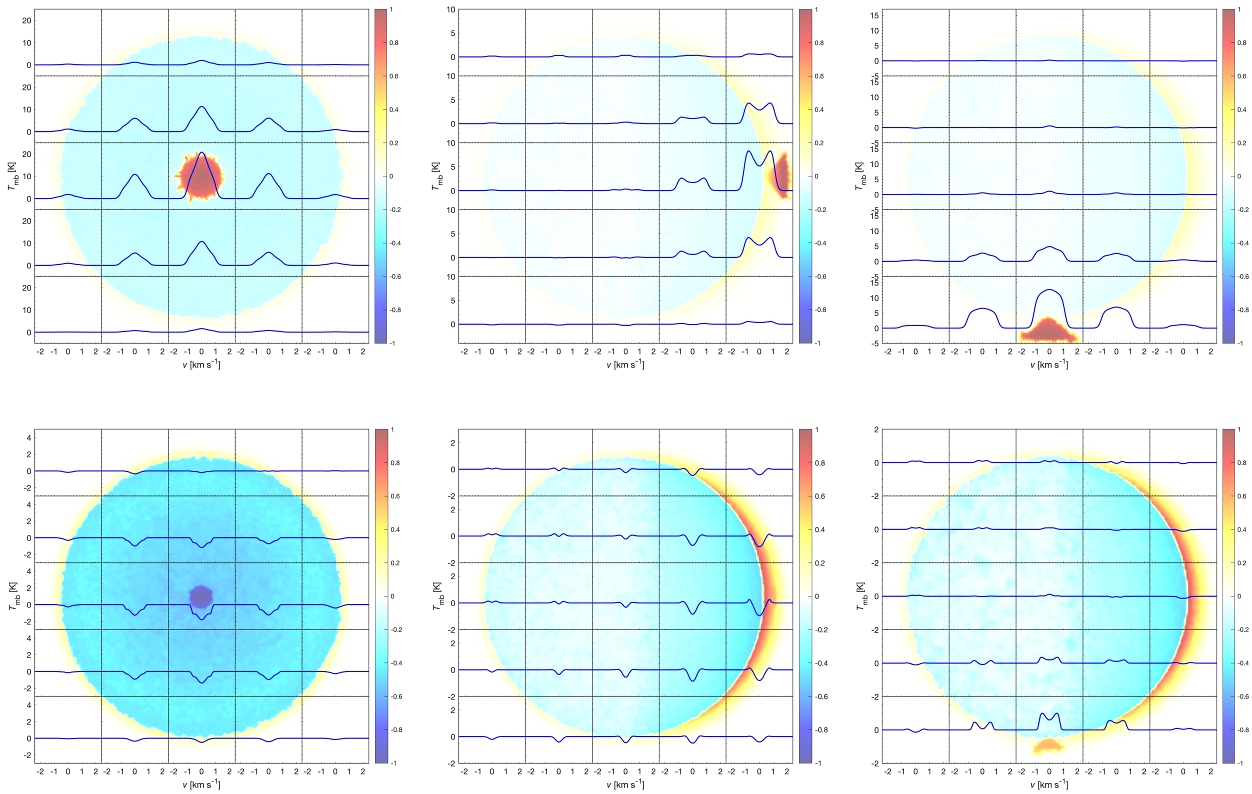

Fig. 9. Five-by-five maps of Ganymede for different plume temperatures. The top row shows models with a plume temperature of 300 K, while the bottom row shows the corresponding models with a plume temperature of 75 K. From left to right, the panels show the difference spectra for CaseIII a0, CaseIII c0, and CaseIII c90. The colour bar indicates the integrated intensity, T_{int}, normalised to the absolute maximum value. The map coordinates in all panels are the same as the upper-left panel in Figure 3, representing CaseIII a0.

central-right panels of Figure 10). In particular, the difference between the spectra with and without the plume reaches values of about 50 K in CaseIII a0, while it is around 30 K in CaseIII b0. This behaviour is similar to what was observed in the base model plume.

In the lower-left panel, we show CaseIII c0, where a macroscopic velocity dispersion of 500 m s^{-1} was applied to the plume. As expected, unlike the radial velocity cases, the spectral feature broadens instead of shifting, with stronger and broader emission wings, showing a temperature difference of more than 2 K compared to the base model in Figure 4. These results clearly show that plume velocity structures can cause both line shifts and broadening in the observed spectra, so precise measurement of the line shapes can also provide information on the active plumes.

4. Discussion

In our radiative transfer model we consider Ganymede as a blackbody emitter with a maximum surface temperature of 150 K at the SSP, which is higher than most of its tenuous water-rich atmosphere. The plume temperature chosen for the base model is also 150 K, which minimises the temperature difference between background and plume when localised at the SSP (the plume area is seen to contribute very weakly in the high-resolution colourmap of Fig. 3), but causes the plume to contribute with emission against the moon background when localised at 45° (Fig. 5) or 180° (Fig. 7). A plume hotter than the background surface enhances the detectability of the emission line wings, such that a 300 K plume results in wing peak emission of up to 10 K, a feature that becomes even more pronounced when observed close to the limb.

As expected, a plume of lower water gas temperature than the background surface results in a lower excitation temperature of the 557 Gz line and thus stronger absorption (see the lower-left map in Fig. 9), while one of higher temperature appears in emission, causing even weaker absorption in the beam-averaged centre spectrum, as shown in the upper-left map of Fig. 9. Recent characterisation of the thermal properties of Ganymede's surface based on JWST observations show SSP temperatures in the range 150–160 K and some variation between leading and trailing side (Bockelée-Morvan et al. 2024), which will have some effect on both excitation and line formation. However, it is beyond the scope of this paper to explore such variations in detail.

The spectra obtained in the five-by-five maps represent spatial averages of the radiative contributions within the SWI instrument's beam. Consequently, even with a plume present in the beam towards the moon surface background, contributing with emission, the absorption contribution from the surrounding atmosphere may dominate and result in a pure absorption spectrum (see e.g. upper-left panel of Fig. A.1). This makes it difficult to identify, unless the plume has a different velocity structure, shifting the emission/absorption as demonstrated in Fig. 10. Furthermore, the higher atmosphere above the plume, extending approximately 200 km in the base model, causes some additional absorption when observed against the moon and plume background.

However, for atmospheric or plume water at the limb of the moon, the line-of-sight column density increases, and the integrated intensity background colour maps always show emission

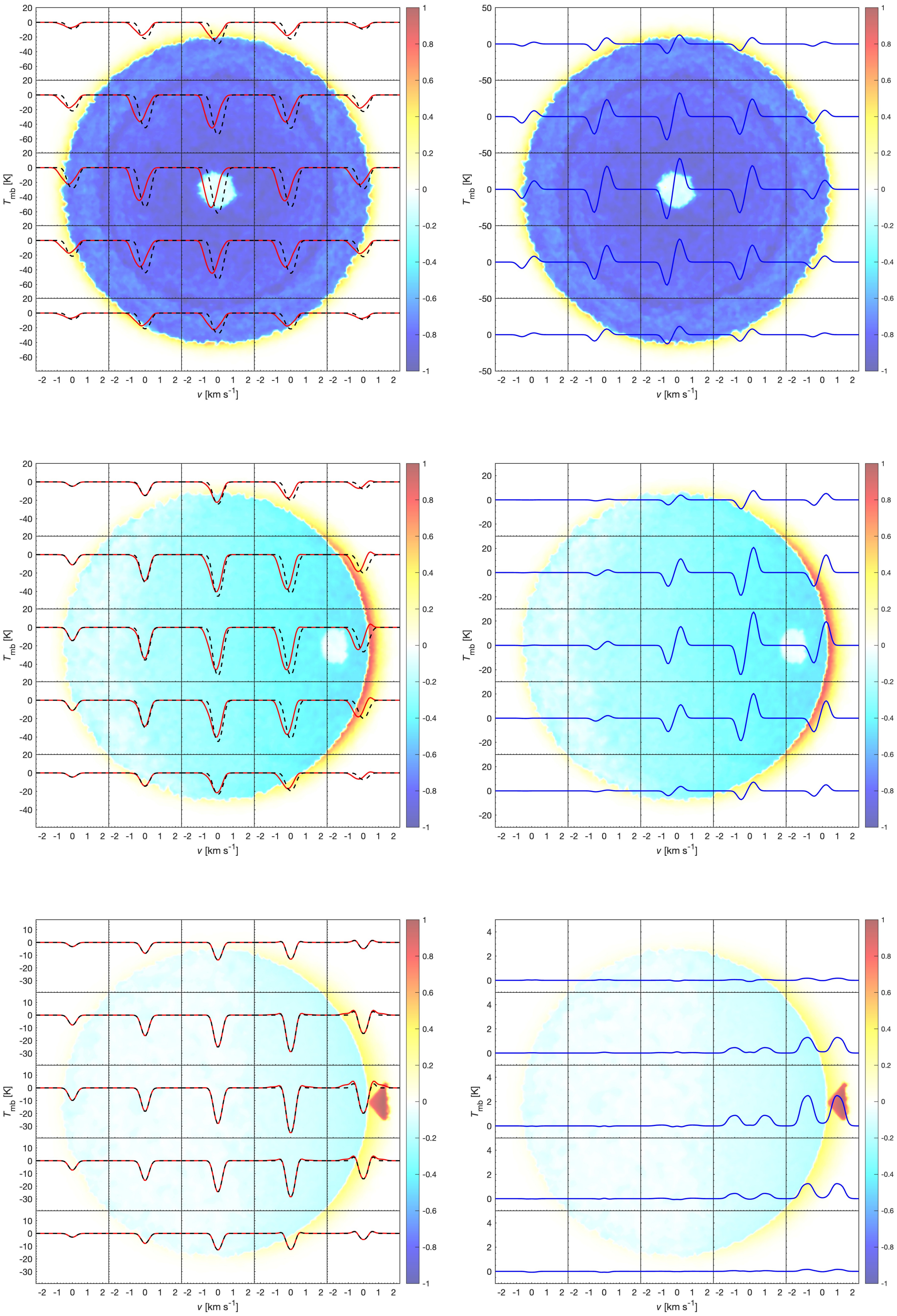

Fig. 10. Five-by-five maps of Ganymede for different plume velocities. The *upper-left panel* and the *centre-left panel* show CaseIII a0 and CaseIII b0 with a radial velocity of the plume set to 500 m/s. The *lower-left panel* presents CaseIII c0, where a Doppler velocity of 500 m/s was introduced. The right panels display the corresponding difference spectra. The colour bar indicates the integrated intensity, T_{int}, normalised to the absolute maximum value. The map coordinates in all panels are the same as the *upper-left panel* in Figure 3, representing CaseIII a0.

– most prominently when observed from 90° phase angle, e.g. in the lower-left map of Fig. 3. In this geometry, even the atmospheric model without a plume (dashed black line) exhibits emission wings in the beam averaged spectra towards the limb, whereas such wings are not obvious when observing the illuminated side of the moon where the absorption contribution is relatively stronger (see upper-right panel of Fig. 3). The presence of a water plume at the limb further amplifies this effect, introducing a localised, denser, and hotter gas source that adds additional emission. This reduces the depth of the absorption lines and increases the intensity of the emission line wings (see the lower-left panel of Fig. 4 and the right map of Fig. 5).

More importantly, there are specific cases in which the emission wings appear exclusively in the presence of a plume and are completely absent in the atmospheric model without the plume. The exact shape and extent of these wings, however, depend on the plume opening angle and outflow velocity. Among these, CaseIII c90, CaseIII e90 and CaseIII c180 stand out as particularly favourable scenarios, showing a $\Delta T_{\max}$ of 4 K, as reported in Table 4. This suggests that the detection of emission wings close to the limb, particularly in observing geometries where no atmospheric water enhancement is expected from other processes, may serve as a key observational indicator of plume activity in SWI measurements. It will be possible for SWI to detect line wings caused by a plume of this type – characterised by a $\Delta T_{\max}$ of 4 K – at a signal-to-noise ratio of 7 in only 10 minutes integration time using its high-resolution Chirp Transform Spectrometer, as reported in Table 4.

In addition to the observing geometry, our models show that plume detectability is also sensitive to water gas temperature and velocity distribution, as expected, but less affected by variations in production rates, with the maximum temperature difference increasing by only 0.8 K when the production rate rises from approximately 10^{27} s^{-1} to 10^{30} s^{-1} (Fig. 8). Gas velocities influence the spectral line profile by broadening the emission wings and, in the presence of a radial component, shifting the line position through the Doppler effect.

4.1. Limitations of the plume model

The detectability scenarios discussed in the previous section provide good indications that SWI could potentially identify water plumes on Ganymede under favourable observational conditions. However, it is equally important to consider the limitations of our modelling approach to correctly interpret these results. As part of this preliminary study, we adopted a simplified model based on a static, uniform, conical plume, with the goal of assessing whether such plumes could be detected by SWI from a distance of approximately 1.2×10^6 km from Ganymede. Naturally, these assumptions do not fully account for the complexities of a real water plume. Hydrodynamic effects, for instance, are expected to produce more complex plume shapes, with velocity, density and temperature gradients. This will likely affect the shape of the spectral lines and the intensity of the emission to some extent. In addition, our model does not take into account possible variations in gas properties due to turbulent mixing or asymmetric venting. To provide a more accurate representation, future studies could consider these factors, which could improve both the precision of the model and our understanding of the dynamics and spectral signature of the plume. This will be particularly important if SWI detects plumes during the moon monitoring phase of the mission and is able to observe them at higher spatial resolution, as a more detailed model will be necessary to correctly interpret the spectral signatures and characterise the plume properties.

Another important aspect is that there are significant uncertainties in the atmosphere model of Marconi (2007), which are propagated to the smoothed water density and temperature profiles used for Ganymede's background atmosphere here. In addition, the current model does not take into account the spatially variable surface properties of Ganymede, including composition, albedo, thermal inertia, etc. Consequently, we do not expect it to be possible to produce difference spectra such as the ones presented here from a combination of this model and SWI data. Actual SWI maps will also likely exhibit additional spectral shape variations caused both by surface properties and atmospheric composition variations and gradients, potentially masking subtle plume signatures. While we still argue that the detection of asymmetric line profiles or wide line wings, especially if large in magnitude and/or transient in time series of maps, will enable the detection and identification of potential plumes also without detailed difference spectra, a more accurate baseline model of the atmosphere and surface radiation properties would be needed to identify less obvious plume signatures. For this, the published 3D Monte Carlo models of Ganymede's atmosphere by Plainaki et al. (2015) or Leblanc et al. (2017) could be a good starting point. It is also important to note that one of the science goals of SWI is to characterise the 3D structure of Ganymede's neutral atmosphere, including its sources and sinks, and thus SWI will contribute towards making a significant improvement in the accuracy of current atmospheric models.

4.2. Implications for SWI moon monitoring strategy

Of the Galilean moons, only Europa has shown observational signatures of water plumes, and they appear to be transient in nature rather than persistent as the plumes emerging from the south pole of Enceladus, feeding the E-ring of Saturn (Villanueva et al. 2023). Being a remote sensing instrument with some capability to direct its antenna independently of the JUICE spacecraft boresight, SWI is planned to use about one hour per 24 h block during the Jupiter tour for moon monitoring observations. This will result in time series of water spectral line moon maps, observed from different phase angles, similar to the model maps presented here. In principle, based on this Ganymede model, we show that there will be two different possibilities to detect water plumes during the moon monitoring: Either SWI detects localised water emission line wings of a magnitude that cannot be explained by other water atmosphere-generating processes or localised variations in line strengths are identified by comparing moon water spectral maps of similar resolution and observing geometry taken at different times, indicating the presence of transient water sources. In both of these scenarios, the general location of the plumes will be identified, and the moon monitoring thus benefits the overall JUICE mission science goals by informing the following detailed planning of observations with all instruments.

The simulations presented here also show that using the daily one hour observing blocks for dedicated, deeper integration maps would increase the possibility of identifying both transient and persistent plumes with SWI. This compared to observing several moons per observing block, resulting in more frequent but noisier maps. In general, they also demonstrate the need for such simulations to study more of the detailed operation scenarios for SWI to refine observing strategies for specific science goals.

5. Conclusions

In this work, we have assessed the feasibility of detecting water plumes in Ganymede's tenuous atmosphere with the SWI instrument on board JUICE from a distance of 1.2×10^6 km from Ganymede, focusing on the 557.936 GHz water line transition. Making use of the 3D radiative transfer code LIME, we analysed different observational geometries to provide a first-order framework for plume detection strategies. Our main findings are as follows:

1. We find that SWI is capable of detecting plume signatures even at production rates of 10^{27} s^{-1} as long as the geometry and plume conditions are favourable. This demonstrates the power of SWI to detect and localise water plumes even from considerable distances – enabling a more strategic planning of observations during moon flybys. Our model results also suggest that recurring deeper integration maps of roughly 5 to 10 minutes per position may increase the likelihood of capturing both persistent and episodic plume events;
2. Plume detection is particularly favoured in two distinct circumstances. The first occurs when the plume is observed at the limb of Ganymede. In these cases, the low background temperature (2.73 K) and the increase in atmospheric path length enhance the visibility of emission features in the spectra. The second occurs in specific cases – such as when the plume is located at 90° from the SSP and SWI observes from 90° or 180°, or when the plume at 180° (backside of the moon) is observed from 90°. In these geometries, the presence of the plume induces strong emission line wings that are absent in the no-plume model. As a result, the temperature difference between the plume and no-plume models in the line wings reaches the highest values at up to ~4 K, making these cases particularly promising for detecting water plumes. A high signal-to-noise ratio, reaching values up to seven, supports the detection of such line wings with 10-minute integrations in the high-resolution SWI mode, assuming a production rate of 10^{29} mol/s;
3. Plume detectability is strongly enhanced by higher gas temperatures. Warmer plumes contribute more significantly to the line emission, making the emission wings more prominent and easier to distinguish from the continuum. Simulations with a 300 K plume show intensity enhancements of 10–20 K compared to the base model, particularly through more pronounced emission wings. In contrast, for cooler plumes (75 K), the signal becomes much weaker, and the emission wings present a very low intensity (<1 K);
4. The velocity of the gas within the plume affects both the shape and the position of the spectral line. Radial velocities can shift the line profile due to the Doppler effect, while thermal or Doppler-like distributions result in broader wings and stronger emission features. These velocity-induced variations may further improve plume detectability.

In summary, our study indicates that SWI can achieve its science goals of detecting water plumes in Ganymede during its routine moon-monitoring segments. A more refined model of the atmosphere and surface radiation properties would make plume identification more reliable, but the modelling framework developed here lays a solid foundation for plume detection on Ganymede and opens the way for analogous investigations of plume activity on icy moons, such as Europa and Callisto, thereby enhancing the scientific return of the JUICE mission.

Acknowledgements. E.S.W. and T.M. acknowledge generous support from the Swedish National Space Agency.

References

Bockelée-Morvan, D., Lellouch, E., Poch, O., et al. 2024, A&A, 681, A27
Brinch, C., & Hogerheijde, M. R. 2010, A&A, 523, A25
Buffa, G., Tarrini, O., Scappini, F., & Cecchi-Pestellini, C. 2000, ApJS, 128, 597
Dayton-Oxland, R., Huybrighs, H. L. F., Winterhalder, T. O., Mahieux, A., & Goldstein, D. 2023, Icarus, 395, 115488
de Kleer, K., Milby, Z., Schmidt, C., Camarca, M., & Brown, M. E. 2023, psj, 4, 37
Fletcher, L. N., Cavalié, T., Grassi, D., et al. 2023, Space Sci. Rev., 219, 53
Fraser, H. J., Collings, M. P., McCoustra, M. R. S., & Williams, D. A. 2001, MNRAS, 327, 1165
Grasset, O., Dougherty, M. K., Coustenis, A., et al. 2013, Planet. Space Sci., 78, 1
Gurnett, D. A., Kurth, W. S., Roux, A., Bolton, S. J., & Kennel, C. F. 1996, Nature, 384, 535
Hall, D. T., Feldman, P. D., McGrath, M. A., & Strobel, D. F. 1998, ApJ, 499, 475
Hansen, G. B., & McCord, T. B. 2004, JGR Planets, 109
Hansen, C. J., Esposito, L. W., Stewart, A. I. F., et al. 2006, Science, 311, 1422
Jia, X., Kivelson, M. G., Khurana, K. K., & Kurth, W. S. 2018, Nature, 2, 459
Kivelson, M. G., Khurana, K. K., Russell, C. T., et al. 1996, Nature, 384, 537
Kivelson, M. G., Khurana, K. K., & Volwerk, M. 2002, Icarus, 157, 507
Leblanc, F., Oza, A. V., Leclercq, L., et al. 2017, Icarus, 293, 185
Ligier, N., Paranicas, C., Carter, J., et al. 2019, Icarus, 333, 496
Mandal, B., & Babikov, D. 2023, A&A, 678, A51
Mandal, B., Żółtowski, M., Cordiner, M., Lique, F., & Babikov, D. 2024, A&A, 688, A1
Marconi, M. L. 2007, Icarus, 190, 155
McGrath, M. A., Lellouch, E., Strobel, D. F., Feldman, P. D., & Johnson, R. E. 2007, in Jupiter, eds. F. Bagenal, T. E. Dowling, & W. B. McKinnon, 457
Orton, G. S., Spencer, J. R., Travis, L. D., Martin, T. Z., & Tamppari, L. K. 1996, Science, 274, 389
Paganini, L., Villanueva, G. L., Roth, L., et al. 2020, Nat. Astron., 4, 266
Pilcher, C. B., Ridgway, S. T., & McCord, T. B. 1972, Science, 178, 1087
Plainaki, C., Milillo, A., Massetti, S., et al. 2015, Icarus, 245, 306
Poppe, A. R., Fatemi, S., & Khurana, K. K. 2018, JGR (Space Phys.), 123, 4614
Porco, C. C., Helfenstein, P., Thomas, P. C., et al. 2006, Science, 311, 1393
Roth, L., Saur, J., Retherford, K. D., et al. 2014, Science, 343, 171
Roth, L., Ivchenko, N., Gladstone, G. R., et al. 2021, Nature, 5, 1043
Saur, J., Duling, S., Roth, L., et al. 2015, JGR (Space Phys.), 120, 1715
Showman, A. P., & Malhotra, R. 1999, Science, 286, 77
Spahn, F., Schmidt, J., Albers, N., et al. 2006, Science, 311, 1416
Sparks, W. B., Hand, K. P., McGrath, M. A., et al. 2016, ApJ, 829, 121
Spencer, J. R. 1987, Icarus, 70, 99
Tian, F., Stewart, A. I. F., Toon, O. B., Larsen, K. W., & Esposito, L. W. 2007, Icarus, 188, 154
Trumbo, S. K., Brown, M. E., Bockelée-Morvan, D., et al. 2023, Sci. Adv., 9, eadg3724
Tseng, W.-L., Lai, I.-L., Ip, W.-H., Hsu, H.-W., & Wu, J.-S. 2022, Universe, 8, 261
Turc, L., Leclercq, L., Leblanc, F., Modolo, R., & Chaufray, J.-Y. 2014, Icarus, 229, 157
Vance, S. D., Styczinski, M. J., Bills, B. G., et al. 2021, JGR Planets, 126, e06418
Villanueva, G. L., Hammel, H. B., Milam, S. N., et al. 2023, Nature, 7, 1056
Vorburger, A., Fatemi, S., Galli, A., et al. 2022, Icarus, 375, 114810
Waite, J. H., Combi, M. R., Ip, W.-H., et al. 2006, Science, 311, 1419
Wirström, E. S., Bjerkeli, P., Rezac, L., Brinch, C., & Hartogh, P. 2020, A&A, 637, A90

Appendix A: Supplementary model spectral maps

This appendix presents additional spectral maps for the different cases and observing geometries discussed in the main text. Figures A.1–A.3 show five-by-five maps of Ganymede for position of the plume at 45°, 90°, and 180°, respectively, observed from different phase angles. Figure A.4 presents the corresponding maps for CaseIII a90, illustrating the impact of different water production rates on the spectral line.

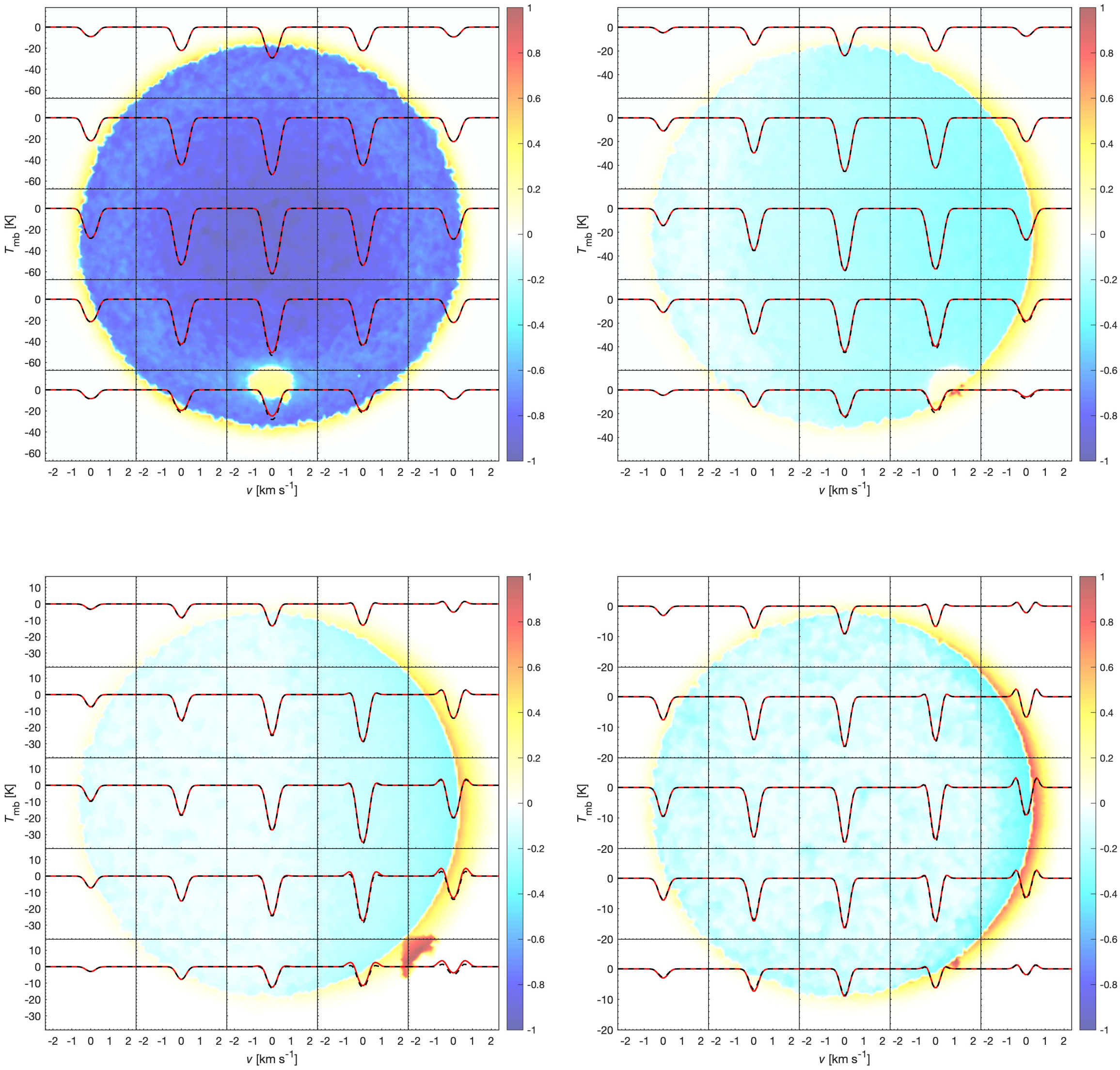

Fig. A.1. Five-by-five maps of Ganymede with the plume at 45°. The *upper-left panel* shows CaseIII a45 with SWI at 0°, the *upper-right panel* displays CaseIII b45 with SWI at 45°, the *lower-left panel* presents CaseIII c45 with SWI at 90°, and the *lower-right panel* depicts CaseIII d45 with SWI at 135°.

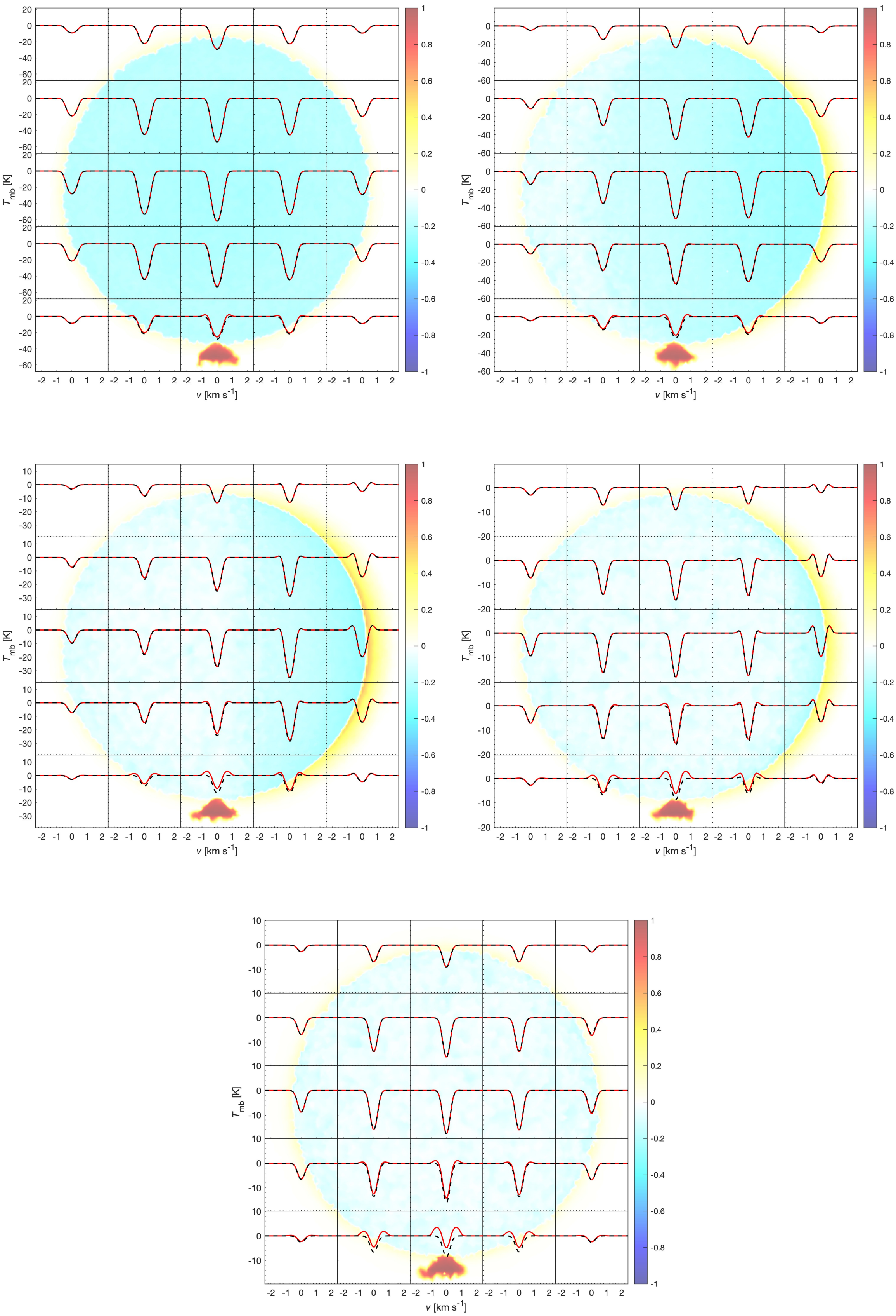

Fig. A.2. Five-by-five maps of Ganymede with the plume located at 90°. The *upper-left panel* shows CaseIII a90 with SWI at 0°, the *upper-right panel* displays CaseIII b90 with SWI at 45°, the *centre-left panel* presents CaseIII c90 with SWI at 90°, the *centre right panel* shows CaseIII d90 with SWI at 135°, and the *bottom panel* displays CaseIII e90 with SWI at 180°, all with respect to the SSP.

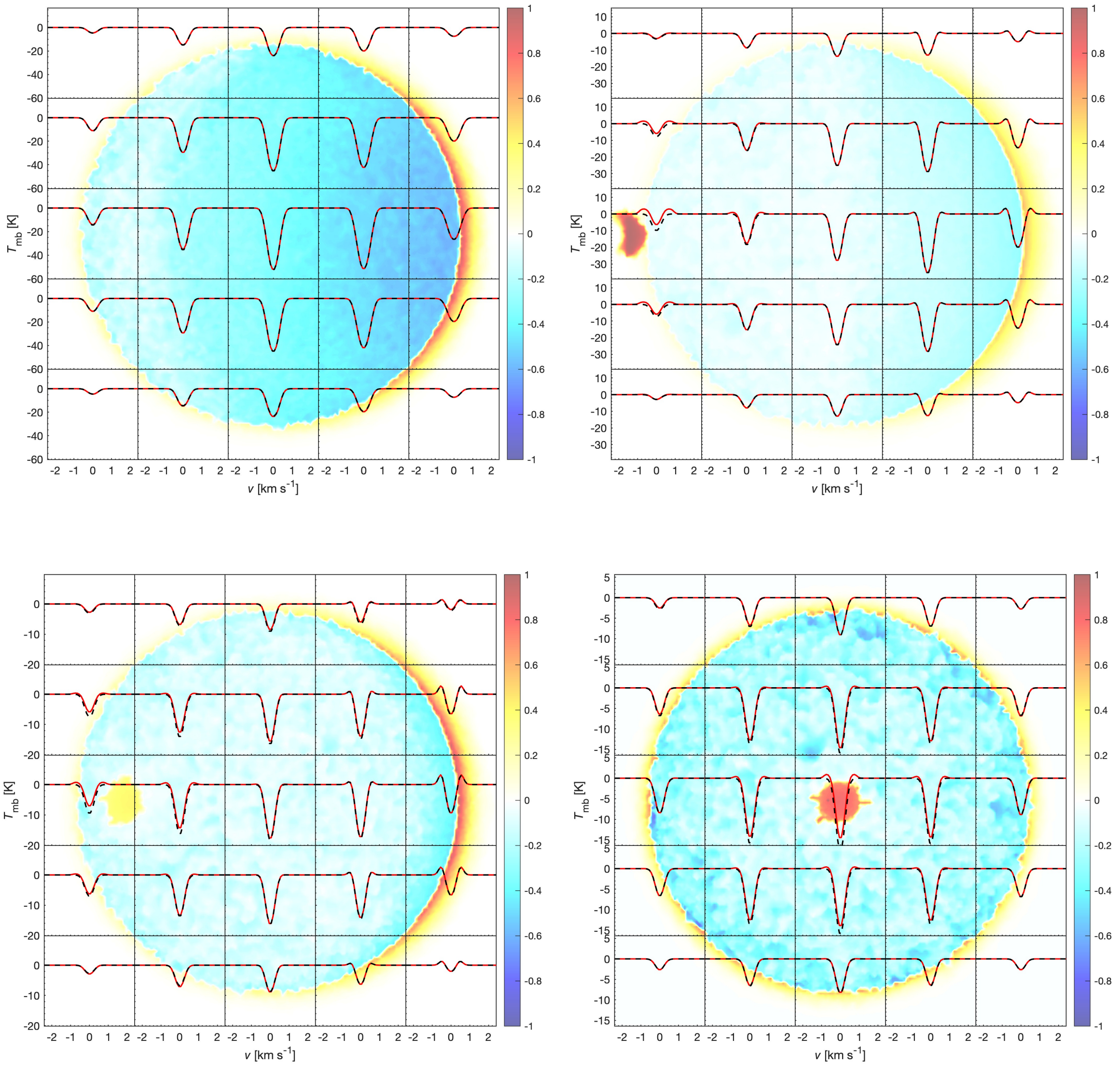

Fig. A.3. Five-by-five maps of Ganymede with the plume located at 180°. The *upper-left panel* shows CaseIII b180 with SWI at 45°, the *upper-right panel* displays CaseIII c180 with SWI at 90°, the *lower-left panel* presents CaseIII d180 with SWI at 135°, and the *lower-right panel* shows CaseIII e180 with SWI at 180°.

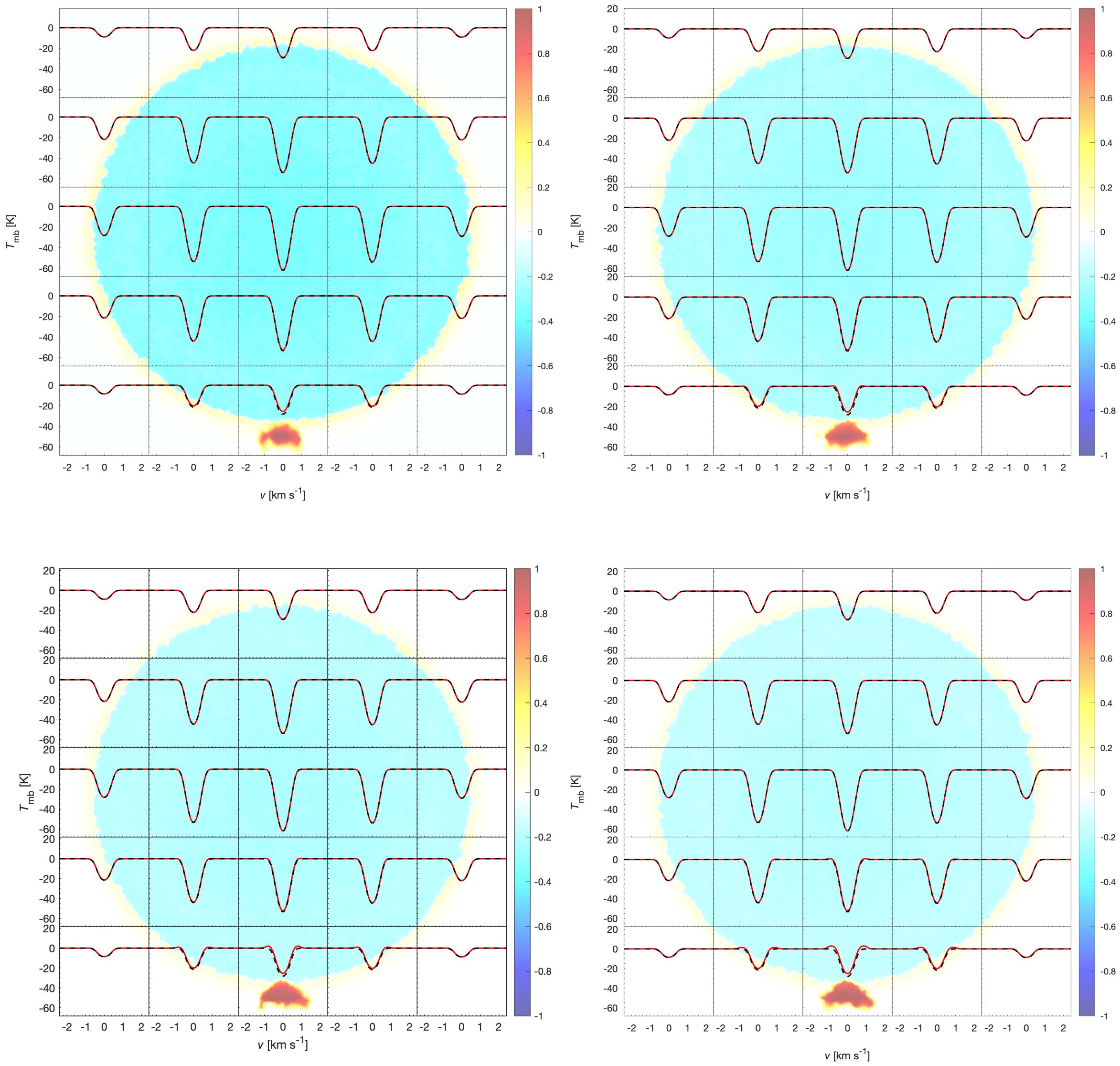

Fig. A.4. Five-by-five maps of Ganymede for CaseIII a90, showing the effect of different water production rates on the observed spectra. The *upper-left panel* corresponds to $Q_1 = 10^{27}$ s^{-1}, the *upper-right panel* to $Q_2 = 10^{28}$ s^{-1}, the *lower-left panel* to $Q_3 = 10^{29}$ s^{-1} (base model), and the *lower-right panel* to $Q_4 = 10^{30}$ s^{-1}.